MOLECULAR IMAGING AND BIOLOGY

Mol Imaging Biol (2017) 19:933–943
DOI: 10.1007/s11307-017-1101-y

Published Online: 13 July 2017

RESEARCH ARTICLE

[^{68}Ga]PSMA-HBED-CC Uptake in Osteolytic, Osteoblastic, and Bone Marrow Metastases of Prostate Cancer Patients

Jan-Carlo Janssen,[1] Nadine Woythal,[2] Sebastian Meißner,[1] Vikas Prasad,[2] Winfried Brenner,[2] Gerd Diederichs,[1] Bernd Hamm,[1] Marcus R. Makowski[1]

[1]*Department of Radiology, Charité, Charitéplatz 1, 10117, Berlin, Germany*
[2]*Department of Nuclear Medicine, Charité, Charitéplatz 1, 10117, Berlin, Germany*

Abstract

Purpose: The aim of this study was to evaluate potential differences in "Glu-NH-CO-NH-Lys" radio-labeled with [^{68}Ga]gallium *N,N*-bis[2-hydroxy-5-(carboxyethyl)benzyl]ethylenediamine-*N,N*-diacetic acid ([^{68}Ga]PSMA-HBED-CC) uptake in osteolytic, osteoblastic, mixed, and bone marrow metastases in prostate cancer (PC) patients.

Procedures: This retrospective study was approved by the local ethics committee. Patients who received [^{68}Ga]PSMA-HBED-CC positron emission tomography/computed tomography ([^{68}Ga]PSMA-PET/CT) with at least one positive bone metastasis were included in this study. Only patients who have not received systemic therapy for their PC were included. Bone metastases had to be confirmed by at least one other imaging modality or follow-up investigation. The maximum standardized uptake value (SUV_{max}) and mean Hounsfield units (HU_{mean}) of each metastasis were measured. Based on CT, each metastasis was classified as osteolytic (OL), osteoblastic (OB), bone marrow (BM), or mixed (M).

Results: One hundred fifty-four bone metastases in 30 patients were evaluated. Eighty out of 154 (51.9%) metastases were classified as OB, 21/154 (13.6%) as OL, 23/154 (14.9%) as M, and 30/154 (19.5%) as BM. The SUV_{max} for the different types of metastases were 10.6 ± 7.07 (OB), 24.0 ± 19.3 (OL), 16.0 ± 21.0 (M), and 14.7 ± 9.9 (BM). The SUV_{max} of OB vs. OL and OB vs. BM metastases differed significantly ($p \leq 0.025$). A significant negative correlation between HU_{mean} and SUV_{max} ($r = -0.23$, $p < 0.05$) was measured.

Conclusions: [^{68}Ga]PSMA-HBED-CC uptake is higher in osteolytic and bone marrow metastases compared to osteoblastic metastases. Information derived from [^{68}Ga]PSMA-PET and CT complement each other for the reliable diagnosis of the different types of bone metastases in PC patients.

Key words: Prostatic neoplasms, Osteoclastic, Osteoblastic, Osseous metastases, Bone marrow metastases, Positron emission tomography, Computed tomography, Tracer uptake, [^{68}Ga]PSMA-HBED-CC

Abbreviations: [^{68}Ga]PSMA-HBED-CC, "Glu-NH-CO-NH-Lys" radio-labeled with [^{68}Ga]gallium *N,N*-bis[2-hydroxy-5-(carboxyethyl)benzyl]ethylenediamine-*N,N*-diacetic acid; [^{68}Ga]PSMA-PET/CT, [^{68}Ga]PSMA-HBED-CC-based positron emission tomography/computed tomography; 2D ROI, Two-dimensional region of interest; OL, Osteolytic; OB, Osteoblastic; M, Mixed; BM, Bone marrow; SUV_{max}, Maximum of standardized uptake value; SUV, Standardized uptake value; BVC, Best valuable comparator; PC, Prostate cancer; [^{99m}Tc]DPD bone scan,

Correspondence to: Jan-Carlo Janssen; *e-mail:* jan-carlo.janssen@charite.de

^{99m}Technetium-3,3-diphospho-1,2-propanedicarbonacid bone scan; CT, Computed tomography; HU, Hounsfield unit

Introduction

Prostate cancer (PC) is the second most common cancer in men worldwide and the most common cancer in males in developed countries [1]. PC metastasizes mostly in bone tissue, representing up to 90% of the overall metastases number [2]. Bone metastases are a major cause of pain and death in PC patients [3]. The metastatic pattern of PC bone metastases has been described to be predominantly osteoblastic; however, also osteolytic, bone marrow, and mixed metastases can be found [4, 5]. The mechanisms underlying these differing metastatic patterns are not fully understood yet. They are dependent on a dynamic cross talk between metastatic cancer cells and bone tissue [5, 6]. Although most PC metastases are radiologically classified as "osteoblastic," the underlying process within the bone metastases includes simultaneously ongoing dysregulated processes of bone resorption (osteoclastic activity) and bone formation (osteoblastic activity) [7–9]. Additionally, osteoclastic cells are, by releasing growth factors out of the bone matrix, a key factor during the growth and migration of PC cancer cells into bone tissues [10]. One of the earliest pathways of PC metastases is the infiltration of the bone marrow, which leads to bone marrow metastases [11]. Bone marrow metastases can represent the earliest detectable form of bone involvement in PC patients. While computed tomography (CT) has a high sensitivity and specificity for the detection of osteoblastic metastases with high Hounsfield units (HU), it has limitations in the detection of osteolytic and bone marrow metastases [12, 13].

Recently, a new promising tracer specific for prostate cancer cells was introduced into the diagnostic workflow of PC patients. Glu-NH-CO-NH-Lys as a prostate-specific membrane antigen (PSMA) radioligand labeled with [^{68}Ga]Ga-*N*,*N*-bis[2-hydroxy-5-(carboxyetyhl)benzyl]-ethylenediamine-*N*,*N* diacetic acid ([^{68}Ga]PSMA-HBED-CC) [14–16]. The high clinical value of this tracer for lymph node staging and local recurrence detection in positron emission tomography/CT ([^{68}Ga]PSMA-PET/CT) was demonstrated in several recent studies [17–19]. Different studies have also demonstrated the potential of this molecular probe for the detection of bone metastases [20, 21].

To the best of our knowledge, there is no data available yet regarding the influence of the different types of bone metastases (osteoblastic, osteolytic, mixed, bone marrow) on the [^{68}Ga]PSMA-HBED-CC tracer uptake in PET. The aim of this study was to investigate potential differences in [^{68}Ga]PSMA-HBED-CC tracer uptake in the different types of bone metastases in PC patients.

Methods

Study Population

This retrospective study was approved by the institutional ethics review board of the Charité University Hospital, Berlin. Inclusion criteria were as follows: (1) patients with confirmed prostate carcinoma and a [^{68}Ga]PSMA-PET/CT examination, (2) at least one bone metastasis was detected in the osseous system, and (3) at least one other imaging modality, confirming the diagnosis of bone metastases ([^{99m}Tc]technetium-3,3-diphospho1,2-propanedicarbonacid bone scan (^{99m}Tc-DPD bone scintigraphy) or magnetic resonance imaging (MRI)), was performed within 4 months for validation. Exclusion criteria were as follows: (1) no validation of bone metastasis through the best valuable comparator (BVC) and (2) any type of therapy (androgen deprivation therapy, chemotherapy, targeted therapy for bone metastases, radiation of bone metastases) except local radiation therapy of the prostate and prostate extirpation. Thereby, therapy effects, which could result in the sclerosis of bone metastases, were excluded. Metastases in the radiation field, in cases of prostate radiation therapy, were excluded from the analysis. Thereby, it was assured that only therapy-naive bone metastases were investigated in our study.

We extracted 719 patients from our imaging database who underwent [^{68}Ga]PSMA-PET/CT between January 24, 2013, and December 13, 2016. Out of these, 109 patients were investigated with at least one other imaging modality in between 4 months and received no therapy except local prostate therapy. Two patients, containing two lesions, could not be validated through BVC and thus were excluded from this study. Thirty patients with at least one bone metastasis were included in this study.

Tracer Acquisition

Gallium-68 was eluted from a standard germanium-68/gallium-68 generator (Eckert & Ziegler Radiopharma GmbH, Berlin, Germany). PSMA-HBED-CC (ABX GmbH, Radeberg, Germany) was labeled with Ga-68 according to the method described previously [14, 22].

Image Acquisition

PET/CT imaging was performed 52.8 ± 23.9 min after intravenous injection of 118.2 ± 19.9 MBq of [^{68}Ga]PSMA-HBED-CC. No significant difference ($p > 0.05$) in mean acquisition time between the four subgroups osteoblastic,

osteolytic, mixed, and bone marrow was found. Therefore, no influence of different acquisition times on SUV_{max} was assumed. All PET scans were acquired in a 3D acquisition mode using a Gemini TF 16 Astonish PET/CT scanner (Philips Medical Systems) [18]. The 3D lines of response algorithm of the system software was used with default parameter settings to reconstruct transaxial, sagittal, and coronal slices (144 voxels with 4 mm^3, isotropic). PET images were acquired from vertex to mid-thigh. Ten to fifteen bed positions were acquired at 1.5 min/bed position with 50% overlapping. A low-dose CT acquired immediately before the PET scan was used for attenuation correction, metastases classification, and anatomical mapping (120 kVp, 30 mAs).

Image Analysis

Visage 7.1 (Visage Imaging GmbH, Berlin, Germany) was used for imaging analysis. PET images were independently analyzed by two observers. Suspicious bone lesions were examined in all three sectional planes (transversal, sagittal, and coronal). A maximum of five lesions per body region (skull, shoulder, humerus, sternum/rib, cervical spine, thoracic spine, lumbar spine, hip, femur) was noted. A PET lesion was regarded to be suspicious for bone metastases if the standardized uptake value (SUV) was higher than the surrounding background. Additionally, to confirm the presence and the location of the metastases, all metastases had to be located in the skeletal system in all three sectional planes. A 2D region of interest (2D ROI) was drawn around the metastases in the sectional plane with the highest maximum SUV (SUV_{max}). The SUV threshold was set to 0–10 for optimal standardization. Every metastasis was visualized again in fused CT images. The CT window was set to center, 500, and width, 1500 HU. Based on the CT data set, each metastasis was classified to be osteoblastic (HU higher compared to surrounding bone tissue, Fig. 1), osteolytic (HU lower than surrounding bone tissue, Fig. 2), mixed (lesion contained both characteristics), and bone marrow metastases (on CT, no changes in the sclerotic structure of the bone marrow could be delineated, Fig. 3). Thus, metastases were divided into four groups: osteoblastic (OB), osteolytic (OL), mixed (M), and bone marrow (BM) metastases. Additionally, a 2D ROI was drawn around each metastases in CT and the minimum, maximum, and mean HU within the respective 2D ROI was noted. Drawing of 2D ROI in PET images enabled the generation of the following quantitative parameters.

SUV_{max}

The uptake of [^{68}Ga]PSMA-HBED-CC was measured by the SUV_{max} in the respective 2D ROI. This parameter was calculated according to the following formula:

$$SUVmax = Q1 \text{ x } BW/Qinj$$

$Q1$ = *Activity within the* ROI *in* MBq / ml at *the acquisition time*
$Qinj$ = *decay-corrected injected dose* at *the acquisition time in* MBq
BW = *Body weight of the patient in* kg

Best Valuable Comparator

As no histological confirmation of bone metastases was available, a best valuable comparator (BVC) was created as a reference standard. The BVC was based on a consensus review of all available imaging studies (MRI, [^{99m}Tc]DPD-single-photon emission computed tomography and bone scan, CT, follow-up [^{68}Ga]PSMA-PET/CT). The mean difference of days between the PET, MRI, and [^{99m}Tc]DPD-SPECT was 33.5 ± 31.8 days.

If there was no indication of bone involvement at the respective location through information of clinical follow-up or other imaging studies, the PET-positive lesion was regarded to be indeterminate. In those cases, the respective lesions were excluded from this study.

Classification of Patient Groups Regarding the Type of Osseous Metastases

For patient characterization, each patient was classified to be part of one of the following groups depending on the most prevalent type of osseous metastases that could be detected in the osseous system of the patient: osteoblastic (OB), osteolytic (OL), or bone marrow (BM). If no "most prevalent" type of lesion could be defined in the respective patients, the patient was classified as mixed (M).

Statistics

All values are given as mean ± standard deviation. SPSS 24 (IBM, Armonk, USA) was used for statistical analysis. The significance of differences in means of SUV_{max}, acquisition time, and PSA levels between the OB and the OL, M, and BM groups was calculated using the Mann-Whitney U test. Correlations were tested with Spearman rho correlation. Normal distribution was tested by using the Kolmogorov-Smirnoff test. As multiple testing on significance was used, the alpha level for statistical significance was calculated through the Bonferroni-Holm method. Therefore, the alpha level for OB vs. OL was regarded to be statistically significant if its value was less than 0.05; for OB vs. BM, less than 0.025; and for OB vs. M, less than 0.0125.

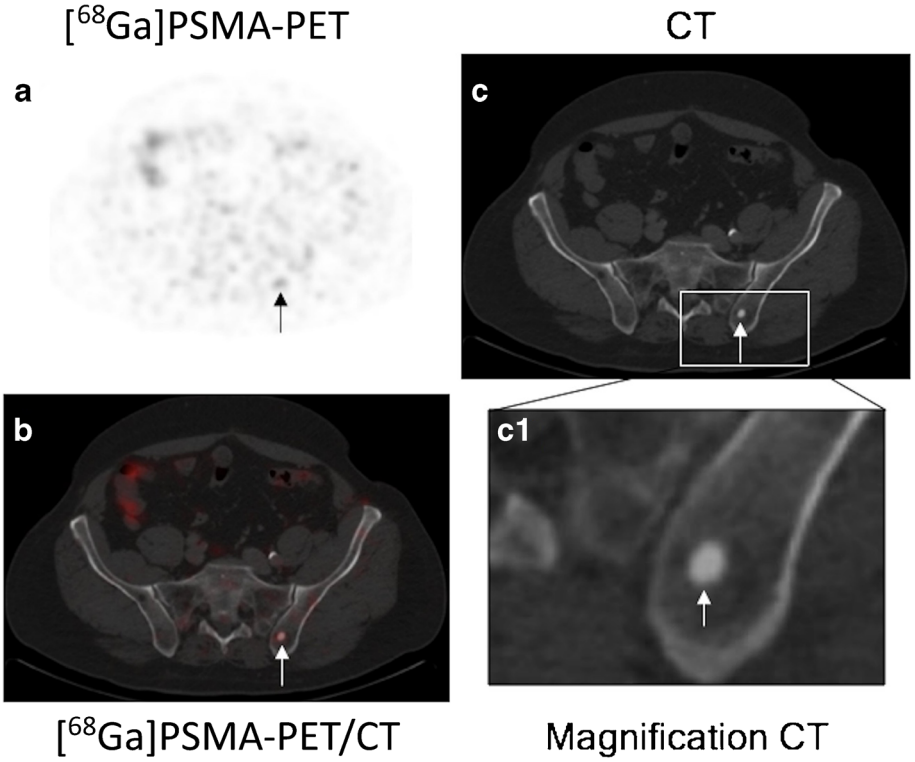

Fig. 1 Example of an osteoblastic bone metastasis in the left Os ilium with a relatively low [^{68}Ga]PSMA-HBED-CC uptake. Example of patient with a focal osteoblastic metastasis (*arrow*) in the dorsal part of the left Os ilium. **a** In the [^{68}Ga]PSMA PET, only a relatively low [^{68}Ga]PSMA uptake can be visualized. **b** In the fused [^{68}Ga]PSMA PET/CT image, the low uptake of the tracer colocalizes with an osteoblastic metastasis. The SUV_{max} of the bone metastasis was 3.0, and the HU_{mean} was 455. **c** On the CT image, the focal osteoblastic metastasis can be clearly visualized (magnification in *c1*). The BVC evaluation was based on a follow-up [^{99m}Tc]DPD-SPECT and rising PSA levels. Five further osseous metastases were detected in this patient.

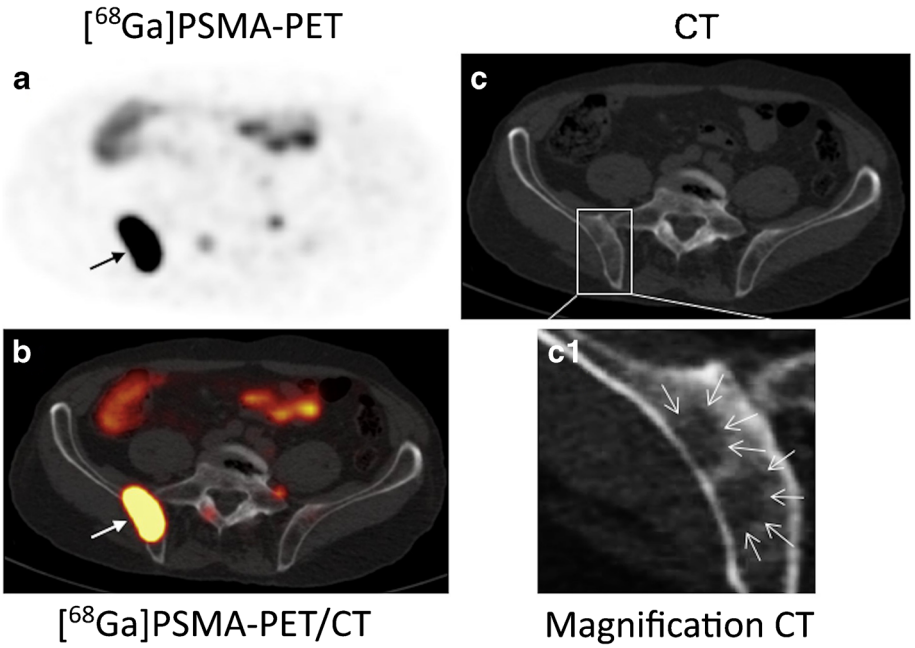

Fig. 2 Example of an osteolytic bone metastasis in the right Os ilium with a strong [^{68}Ga]PSMA-HBED-CC uptake. Example of a patient with a focal osteolytic metastasis (*thick arrow*) in the dorsal part of the right Os ilium. **a**, **b** In the [^{68}Ga]PSMA PET image, an area with a strong [^{68}Ga]PSMA uptake is visualized. The SUV_{max} of the lesion was 61.9, and the HU_{mean} was 87.8. **c** The corresponding CT image shows a corresponding diffuse osteolytic lesion in the right part of the right Os ilium (magnification *c1*, *thin arrows*).

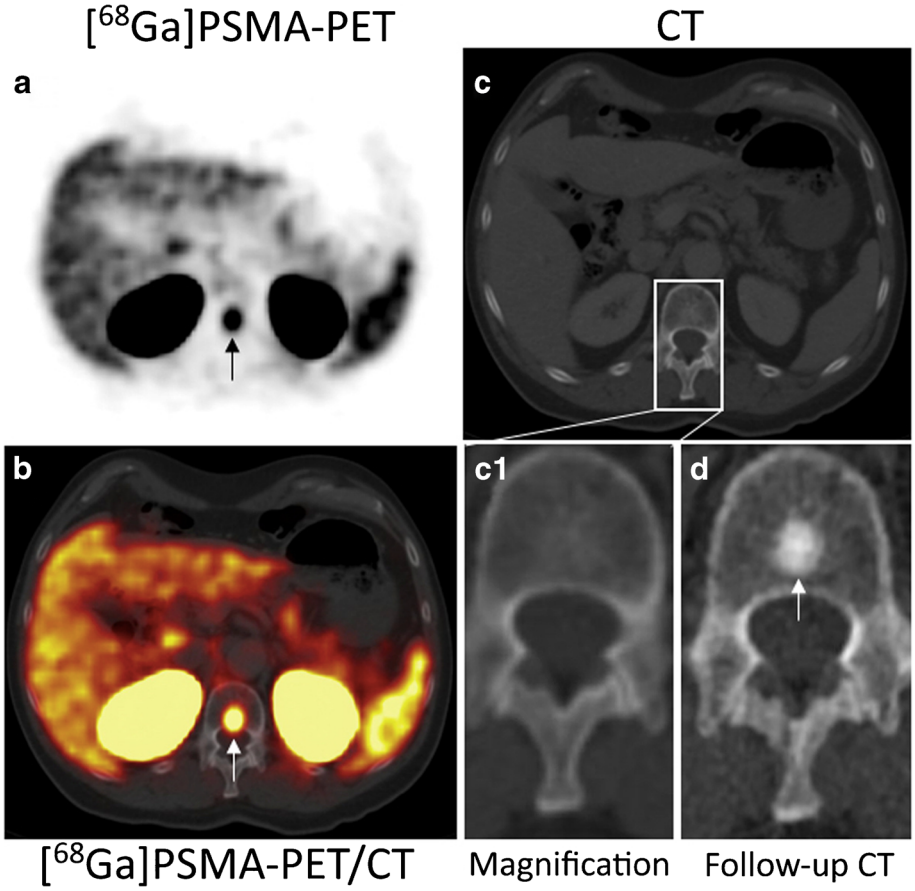

Fig. 3 Example of a bone marrow metastasis in a lumbar vertebral body with a strong [^{68}Ga]PSMA-HBED-CC uptake, which is not visible on computed tomography. **a–c** Example of a patient with a bone marrow metastasis and associated strong [^{68}Ga]PSMA-HBED-CC uptake. **a**, **b** In the [^{68}Ga]PSMA PET/CT image, a focal strong PSMA uptake is visualized in the dorsal part of the first lumbar vertebral body (*black and white arrow*). The metastasis had a SUV_{max} of 29.1. **c** On the CT image, the PET-positive metastasis does not show any changes in the calcified bone marrow structure of the lumbar vertebral body (magnification *c1*). The bone marrow metastasis would therefore have been missed on the CT data set. **d** In the follow-up CT examination 18 months later, a clear osteoblastic bone metastasis can be visualized in this area on CT.

Results

Characterization of Bone Metastases in Patients with Prostate Cancer

In total, 156 PET-positive lesions were detected. Out of these, 154 lesions were confirmed through BVC (98.7%). Two patients, containing two lesions, were regarded to be indeterminate and thus were excluded from this study. For a detailed evaluation of the distribution of the bone metastases, see Table 1. In the OB, OL, and M groups, the hip was the predominant region in which bone metastases were detected (42 out of 124 metastases). For the BM group, the rib/sternum region was the predominant region in which bone metastases were detected (9 out of 30 metastases). In the humerus, only a small number of osteoblastic metastases were detected (3 out of 154 metastases). Overall, the pelvis was the most prevalent region for bone metastases (46 out of 154 metastases). The second most prevalent region was the lumbar spine (33 out of 154 metastases). The skull was the only region in which no bone metastasis was detected.

For a detailed summary of the distribution of metastases in the skeleton system, please refer to Table 1.

Patient Characteristics

Thirteen out of 30 patients demonstrated predominantly osteoblastic metastases. Their mean age was 66.2 ± 6.4 years, and their mean prostate-specific antigen (PSA) level was 43.2 ± 75.5 ng/ml. Five out of 30 patients demonstrated predominantly osteolytic metastases. Their mean age was 70.2 ± 5.4 years. They had the highest PSA level with 66.5 ± 84.6 ng/ml (in comparison to OB, M, and BM). Differences, however, did not reach statistical significance ($p > 0.05$). Seven out of 30 patients demonstrated predominantly mixed metastases, or they had no

Table 1. Summary of anatomical distribution of bone metastases in patients with prostate cancer

Location	Type of metastasis				
	Osteoblastic	Osteolytic	Mixed	Bone marrow	Total
Skull	–	–	–	–	–
Scapula/clavicula	5	1	1	3	10
Humerus	3	–	–	–	3
Rib/sternum	15	1	2	9	27
Cervical spine	6	2	1	1	10
Thoracic spine	9	3	2	3	17
Lumbar spine	14	5	6	8	33
Hip	24	7	11	4	46
Femur	4	2	–	2	8
Total	80	21	23	30	154

This table summarized the distribution of bone metastases in the skeletal system (rows) and the associated classification based on CT Hounsfield units (columns). The column on the right represents the overall number of bone metastases independent from their classification. The bottom row represents the overall number of bone metastases independent from the body region they were detected in. Most osseous metastases were detected in the spine and the pelvis

– no findings in the respective body region, *bone marrow* bone marrow metastases

predominant type of metastases. Five out of 30 patients demonstrated predominantly CT-negative bone marrow metastases. For details, please refer to Table 2.

Osteoblastic, Osteolytic, Mixed, and CT-Negative Lesions

Eighty of 154 (51.9%) metastases were classified to be osteoblastic, based on the CT data set. Osteoblastic lesions demonstrated the lowest mean SUV_{max} with 10.6 ± 7.1 with a range of 2.3 to 34.5 (95% CI 9.1–12.2). An example of a metastasis with a relatively low SUV_{max} and a high HU is demonstrated in Fig. 1.

Twenty-one of 154 (13.6%) metastases were classified to be osteolytic based on the CT data set. A mean SUV_{max} of 24 ± 19.3 with a range of 4.2–61.9 (95% CI 15.2–32.8) was measured. An example of a metastasis with a relatively high SUV_{max} and a low HU value is demonstrated in Fig. 2.

Twenty-three of 154 (14.9%) metastases were classified to be mixed. Their mean SUV_{max} was 16.0 ± 21.0 with a range of 2.8–104.4 (95% CI 6.9–25.0). This group of metastases had the highest standard deviation.

For 30 of 154 (19.5%) metastases, no changes in the sclerotic structure of the bone marrow could be delineated on CT. Those metastases were classified as bone marrow metastases. The mean SUV_{max} of the BM group was 14.7 ± 9.9 with a range of 2.7–48.4 (95% CI 11–18.4). An example of a metastasis with a relatively high [^{68}Ga]PSMA-HBED-CC uptake and no correlate on CT images is demonstrated in Fig. 3.

Comparison of Means of SUV_{max}

A significant difference in means of SUV_{max} between the osteoblastic and the osteolytic groups ($p = 0.001$; $U = 451$) and between the osteoblastic and bone marrow groups ($p = 0.025$; $U = 866.5$) was measured. Although the mean SUV_{max} of the mixed group was measured to be higher compared to the OB group, no significant difference ($p = 0.37$; $U = 807$) was detected. Additionally, no significant difference for the following comparisons was measured: OL vs. M, OL vs. BM, and M vs. BM ($p > 0.05$). For a summary of the results, please refer to Table 3. Figure 4 demonstrates a box plot depicting the SUV_{max} values of the different groups.

Correlations of SUV_{max} and HU_{mean} and HU_{max} and HU_{min}

For testing the correlations between SUV_{max} and HU values, only OB and OL metastases were analyzed. The assessment was limited to these types of osseous metastases as mixed metastases demonstrated a high variance of HU values. CT-negative lesions (BM) were excluded as no corresponding changes could be delineated on the CT images.One hundred one out of 154 lesions were included in this analysis. Spearman's rho correlation of SUV_{max} and HU_{mean} resulted in a negative correlation coefficient of −0.23 ($p < 0.05$). Figure 5 shows a scatter plot demonstrating the distribution

Table 2. Patient characteristics regarding the different types of metastases

Type of metastases	Age of the patients		PSA level (ng/ml)		Number of patients
	Mean	SD	Mean	SD	
Osteoblastic	66.2	6.4	43.2	75.5	13
Osteolytic	70.2	5.4	66.5	84.6	5
Mixed	68.7	7.7	52.2	58.5	7
Bone marrow	72.2	6.4	53.2	62.2	5
Total	68.5	6.5	50.8	68.3	30

This table summarizes the age of the patients and their PSA levels (ng/ml) with regard to the different types of bone metastases. The bottom row summarizes the characteristics of all patients. No significant difference ($p > 0.05$) in PSA levels were measured between the different patient groups. Values are given as mean with standard deviation

SD standard deviation

Table 3. Summary of SUV_{max} values for the different types of bone metastases

Type of metastases	Mean SUV_{max}	SD	Range	95% CI	*p*-value		
					OB vs. OL	OB vs. M	OB vs. BM
Osteoblastic	10.6	7.1	2.3–34.5	9.1–12.2	<0.05	>0.0125	≤ 0.025
Osteolytic	24.0	19.3	4.2–61.9	15.2–32.8			
Mixed	16.0	21.0	2.8–104.4	6.9–25.0			
Bone marrow	14.7	9.9	2.7–48.4	11.0–18.4			
Total	14.0	13.3	2.3–104.4	11.9–16.2			

The mean SUV_{max} values are demonstrated in combination with the different metastatic classifications of bone metastases. The three columns on the right demonstrate *p* values based on the Mann-Whitney *U* tests, comparing mean SUV_{max} of osteoblastic vs. osteolytic, osteoblastic vs. mixed, and osteoblastic vs. bone marrow metastases. Standard deviation, range, and 95% confidence intervals are given for the respective SUV_{max} values.
OB osteoblastic, *OL* osteolytic, *M* mixed, *BM* bone marrow metastases, *SD* standard deviation, *CI* confidence interval

of HU_{mean} and SUV_{max} values. The SUV_{max} and HU_{min} were demonstrated to have a negative correlation coefficient of −0.198 ($p < 0.05$). The correlation of SUV_{max} and HU_{max} was not significant with a correlation coefficient of −0.160 ($p = 0.11$).

Discussion

This study demonstrated several novel findings for the characterization of bone metastases in PC patients by [^{68}Ga]PSMA-PET/CT: (1) An increased [^{68}Ga]PSMA-HBED-CC uptake can be measured in all types of bone metastases; (2) osteolytic and bone marrow lesions demonstrated a significantly higher [^{68}Ga]PSMA-HBED-CC uptake compared to osteoblastic lesions; and (3) the [^{68}Ga]PSMA-HBED-CC SUV_{max} value of bone metastases demonstrates a significantly negative correlation with the corresponding HU_{mean} value.

These results are clinically relevant as they underline that [^{68}Ga]PSMA-PET and CT work synergistically for the detection of bone metastases in PC patients. [^{68}Ga]PSMA-PET shows the highest signal in bone marrow/osteolytic metastases, while CT demonstrates the highest Hounsfield units in osteoblastic metastases. Additionally, the results of this study could be relevant for the planning of PSMA-based therapies in patients with bone metastases, as especially bone marrow/osteolytic metastases seem to express PSMA.

Development of Bone Metastases in Patients with Prostate Cancer

Bone metastases are the most frequent type of metastases in PC patients and represent the major cause of pain and death in this patient collective [2, 3]. Different types of bone metastases, including osteoblastic and osteolytic metastases, can be observed in PC patients. The pathobiological reasons for these different metastatic patterns are not fully elucidated yet [5, 6]. Although most bone metastases are associated with an osteoblastic appearance on conventional x-ray and CT, it was suggested that a rapid tumor progression is associated with predominantly osteolytic metastases [23]. Additionally, different studies suggested that osteolytic processes represent a relatively early event in the bone invasion process of metastatic prostate cancer cells [11, 24–26]. It was also shown that osteoclastic activity in bone metastases can be observed prior to osteoblastic activity [3, 27, 28]. Based on these studies, it is assumed that the overall metastatic process in PC patients starts with predominantly osteolytic metastases, which are also an indicator for fast tumor growth. During further development, these metastases develop into a predominantly osteoblastic type of metastases.

The general assumption that prostate cancer is predominantly associated with osteoblastic metastases may have originated from the relatively late time points of the diagnosis and the imaging techniques used in the past. These imaging techniques include x-ray radiography, CT, and [^{99m}Tc]DPD bone scintigraphy, which are all inherently more sensitive for the detection of osteoblastic metastases [12, 13, 29, 30].

Nowadays, sensitive detection methods such as high-resolution 3T MRI or guided prostate biopsies enable the detection of prostate cancer at an early stage of development. As a result of this, more and more osteolytic metastases are detected in this patient collective [5, 23]. Therefore, novel imaging techniques which enable the early reliable detection of osteolytic metastases are needed.

Imaging Modalities for the Visualization of the Different Types of Bone Metastases

Different imaging modalities are available for the visualization of bone metastases. The most reliable modalities currently used in clinical practice are computed tomography (CT), magnetic resonance imaging (MRI), positron emission tomography (PET), single photon emission computed tomography (SPECT), and hybrid modalities such as PET/CT and SPECT/CT.

In CT, osteoblastic metastases demonstrate higher Hounsfield units compared to surrounding bone marrow, while osteolytic metastases are associated with lower Hounsfield

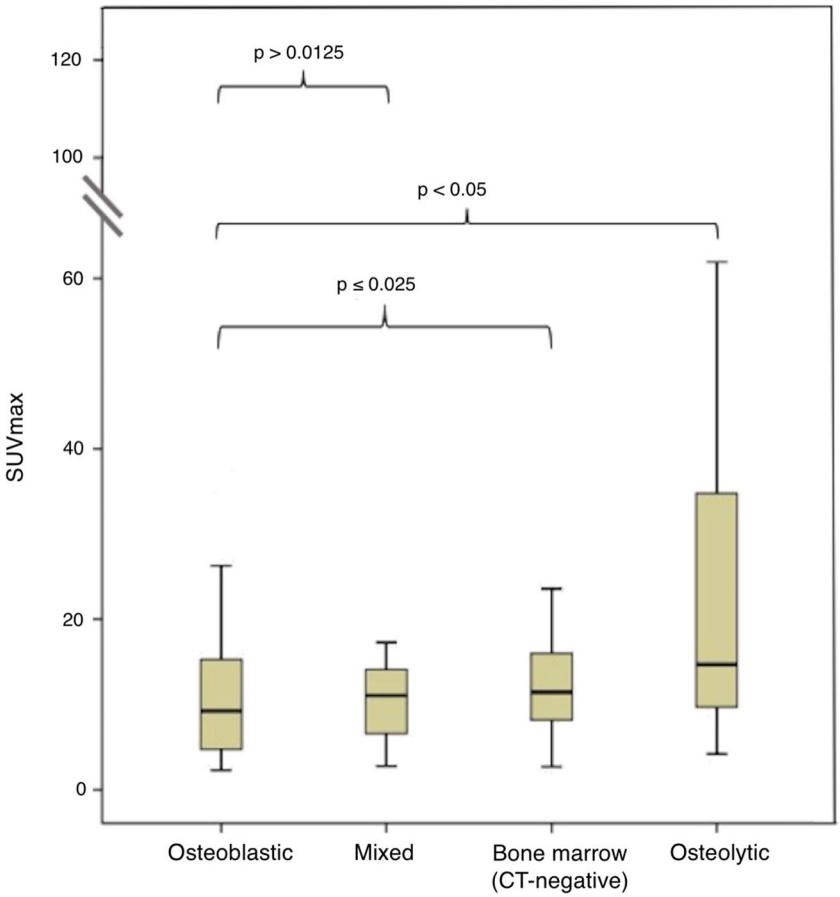

Fig. 4 Box plots demonstrating SUV_{max} values of the different types of bone metastases. Box plots demonstrate the distribution of SUV_{max} values for the different types of bone metastases. A significant difference was measured between osteoblastic metastases and bone marrow (CT-negative) metastases ($p = 0.025$) and between osteoblastic and osteolytic metastases ($p < 0.05$). No significant difference was found between osteoblastic and mixed metastases ($p > 0.0125$). The annotation of the *y-axis* contains SUV_{max} values with a break in between 60 and 100.

units. CT was shown to be especially sensitive for the detection of osteoblastic metastases, as they can be detected as a focal bright spot in the surrounding bone tissue. The sensitivity and specificity of CT for the detection of osteolytic metastases seem to be slightly lower, compared to osteoblastic metastases [12, 13]. In MRI, the detection of especially osteoblastic metastases can also be challenging as this type of metastases can only be visualized with a negative or dark signal in the different MRI sequences.

A recently introduced probe, [^{68}Ga]PSMA-HBED-CC, could help to improve the sensitivity and specificity of the detection of bone metastases [19]. The binding of the Ga-68-labeled small-molecule PSMA inhibitor Glu-NH-CO-NH-Lys(Ahx)-HBED-CC is based on its high affinity to the prostate specific membrane antigen (PSMA). PSMA is a transmembrane protein expressed predominantly in prostate cells and especially in prostate cancer cells [14].

To the best of our knowledge, no previous studies specifically evaluated the potential of [^{68}Ga]PSMA-PET for the visualization the different types of bone metastases. This could be relevant for the clinical staging of patients but also for the evaluation for radioligand therapy based on the expression of PSMA [31].

Potential of [^{68}Ga]PSMA-PET for the Visualization of the Different Types of Bone Metastases

For an optimal therapy planning in PC patients, it is of high importance to reliably detect development of bone metastases as early as possible. Bone marrow metastases are thought to represent the earliest type of bone metastases. In this type of metastases, no reaction of the calcified structures in the bone marrow to the invasion of tumor cells is detectable on CT yet [23, 32]. This study demonstrated that [^{68}Ga]PSMA-PET enables the reliable detection of this type of metastases with a relatively high SUV_{max}. Based on [^{68}Ga]PSMA-PET, this type of metastases could be detected prior to the development of a morphological correlate in CT (Fig. 3).

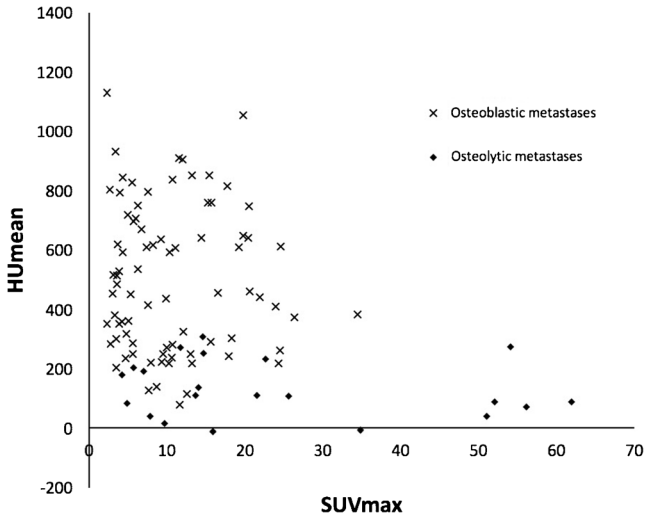

Fig. 5 Scatter plot demonstrating the association of the SUV_{max} value with the HU_{mean} value. The scatter plot demonstrates the association of the SUV_{max} value derived from PET with the HU_{mean} value derived from CT. The osteoblastic metastases are represented by a *cross sign*, the osteolytic metastases by a *square*. It can be appreciated that osteolytic metastases are associated with lower HU_{mean} values and higher SUV_{max} values compared to the osteoblastic metastases. The annotation of the *x-axis* contains SUV_{max} values; the annotation of the *y-axis* shows HU_{mean} values.

Osteolytic metastases also demonstrated a strong uptake of [^{68}Ga]PSMA-HBED-CC, which was higher compared to osteoblastic metastases. The high uptake of [^{68}Ga]PSMA-HBED-CC could be related to a fast tumor growth associated with an increased expression of PSMA and an increased neovascularization of this type of bone metastases. Additionally, a higher number of viable tumor cells in osteolytic and bone marrow metastases, compared to osteoblastic metastases, could explain this difference. A possible explanation for the reduced [^{68}Ga]PSMA-HBED-CC uptake of osteoblastic metastases is the increased calcification of this type of metastases and therefore the smaller percentage of vital tumor cells. Overall, the higher uptake of [^{68}Ga]PSMA-HBED-CC seems to be associated with a higher grade of malignancy and cell turnover of osteolytic and bone marrow metastases compared to osteoblastic metastases. In this context, this study also demonstrated a negative correlation between HU_{mean} and SUV_{max}. Those results underline and confirm our findings, since osteoblastic metastases are associated with high HU values and osteolytic lesions with low HU values. The SUV_{max} between osteoblastic and mixed metastases, however, did not differ significantly.

This study demonstrates that [^{68}Ga]PSMA-PET and CT work synergistically for the detection of metastases in PC patients since the strongest [^{68}Ga]PSMA-PET signal was found in bone marrow/osteolytic metastases while CT demonstrates the highest Hounsfield units in osteoblastic metastases. This underlines that in [^{68}Ga]PSMA-PET/CT, the reader of the image data sets has to specifically focus on the different types of bone metastases in the different imaging modalities to achieve the highest sensitivity and specificity for the detection of metastases in PC patients.

Regarding a radioligand therapy approach based on [^{177}Lu]PSMA therapies [31, 33, 34], a previous study demonstrated that the pretherapeutic [^{68}Ga]PSMA-HBED-CC SUV_{max} value showed a mild correlation with the therapeutic uptake of [^{177}Lu]PSMA [35]. Based on this study, it was hypothesized that predominantly osteolytic or bone marrow metastases could be more responsive to a treatment with [^{177}Lu]PSMA. However, a recent study did find a trend but not a significant correlation of pretherapeutic [^{68}Ga]PSMA-HBED-CC uptake values with therapeutic [^{177}Lu]PSMA uptake [36]. Based on currently available data, no clear conclusion can be drawn regarding this issue. Further studies are now warranted, investigating which collective of patients with which type of metastases benefits most from ^{177}Lu-PSMA therapy.

Limitations

This study is limited by being retrospective. Furthermore, the investigated bone metastases were not validated by histology. To overcome this limitation, the BVC was created. A comparable approach has been taken in other studies concerning the investigation of metastases with PET [21, 37, 38]. To confirm the validity of the BVC used in this study, a subgroup analysis of 24 patients with the most reliable indicators of metastases (MRI, follow-up PET, malign fractures) was performed. No significant difference regarding the conclusions drawn in our manuscript was found between this group and the other patients included in our study. Nevertheless, the BVC does not represent a perfect reference standard. Different reports are available regarding the cases of false positive PSMA uptake which can also be false positive in CT or [^{99m}Tc]DPD-SPECT (e.g., healing fractures, hemangioma, and Paget disease) [39–41]. Keeping this in mind, there is a chance of misinterpreting lesions especially in a small number of patients in this study with no MRI or follow-up PET available. On the other hand, specificity values for [^{68}Ga]PSMA-PET evaluating bone metastases were reported to be 98.8–100% [21] and the high interobserver correlation of Fleiss' kappa = 0.88 for bone metastases [42] suggests a high reliability of [^{68}Ga]PSMA-PET in skeletal staging of PC patients.

Conclusion

[^{68}Ga]PSMA-HBED-CC uptake is higher in osteolytic and bone marrow metastases compared to osteoblastic metastases. Therefore, information derived from [^{68}Ga]PSMA-PET and CT complement each other for the reliable diagnosis of bone metastases in PC patients. Future prospective studies are warranted to investigate the relationship between in vivo [^{68}Ga]PSMA-HBED-CC uptake and the histological malignancy grades of PC bone metastases.

Acknowledgements. MRM is grateful for the financial support from the Deutsche Forschungsgemeinschaft (DFG, 5943/31/41/91).

Compliance with Ethical Standards. This retrospective study was approved by the institutional ethics review board of the Charité University Hospital, Berlin.

Informed Consent

In this retrospective study, written informed consent was waived by the Institutional Review Board.

Conflict of Interest

The authors declare that they have no conflict of interest.

References

1. Torre LA, Bray F, Siegel RL et al (2015) Global cancer statistics, 2012. CA Cancer J Clin 65:87–108
2. Bubendorf L, Schopfer A, Wagner U et al (2000) Metastatic patterns of prostate cancer: an autopsy study of 1,589 patients. Hum Pathol 31:578–583
3. Carlin BI, Andriole GL (2000) The natural history, skeletal complications, and management of bone metastases in patients with prostate carcinoma. Cancer 88:2989–2994
4. Charhon SA, Chapuy MC, Delvin EE et al (1983) Histomorphometric analysis of sclerotic bone metastases from prostatic carcinoma special reference to osteomalacia. Cancer 51:918–924
5. Dushyanthen S, Cossigny DA, Quan GM (2013) The osteoblastic and osteoclastic interactions in spinal metastases secondary to prostate cancer. Cancer Growth Metastasis 6:61–80
6. Ibrahim T, Flamini E, Mercatali L et al (2010) Pathogenesis of osteoblastic bone metastases from prostate cancer. Cancer 116:1406–1418
7. Mundy GR (2002) Metastasis to bone: causes, consequences and therapeutic opportunities. Nat Rev Cancer 2:584–593
8. Roodman GD (2004) Mechanisms of bone metastasis. Discov Med 4:144–148
9. Roudier MP, Vesselle H, True LD et al (2003) Bone histology at autopsy and matched bone scintigraphy findings in patients with hormone refractory prostate cancer: the effect of bisphosphonate therapy on bone scintigraphy results. Clin Exp Metastasis 20:171–180
10. Taichman RS, Loberg RD, Mehra R, Pienta KJ (2007) The evolving biology and treatment of prostate cancer. J Clin Invest 117:2351–2361
11. Jin JK, Dayyani F, Gallick GE (2011) Steps in prostate cancer progression that lead to bone metastasis. Int J Cancer 128:2545–2561
12. Lange MB, Nielsen ML, Andersen JD et al (2016) Diagnostic accuracy of imaging methods for the diagnosis of skeletal malignancies: a retrospective analysis against a pathology-proven reference. Eur J Radiol 85:61–67
13. Evangelista L, Panunzio A, Polverosi R et al (2012) Early bone marrow metastasis detection: the additional value of FDG-PET/CT vs. CT imaging. Biomed Pharmacother 66:448–453
14. Afshar-Oromieh A, Malcher A, Eder M et al (2013) PET imaging with a [^{68}Ga]gallium-labelled PSMA ligand for the diagnosis of prostate cancer: biodistribution in humans and first evaluation of tumour lesions. Eur J Nucl Med Mol Imaging 40:486–495
15. Eder M, Neels O, Muller M et al (2014) Novel preclinical and radiopharmaceutical aspects of [^{68}Ga]Ga-PSMA-HBED-CC: a new PET tracer for imaging of prostate cancer. Pharmaceuticals (Basel) 7:779–796
16. Eder M, Schafer M, Bauder-Wust U et al (2012) ^{68}Ga-complex lipophilicity and the targeting property of a urea-based PSMA inhibitor for PET imaging. Bioconjug Chem 23:688–697
17. Eiber M, Maurer T, Souvatzoglou M et al (2015) Evaluation of hybrid ^{68}Ga-PSMA ligand PET/CT in 248 patients with biochemical recurrence after radical prostatectomy. J Nucl Med 56:668–674
18. Maurer T, Gschwend JE, Rauscher I et al (2016) Diagnostic efficacy of ^{68}Gallium-PSMA positron emission tomography compared to conventional imaging for lymph node staging of 130 consecutive patients with intermediate to high risk prostate cancer. J Urol 195:1436–1443
19. Afshar-Oromieh A, Avtzi E, Giesel FL et al (2015) The diagnostic value of PET/CT imaging with the ^{68}Ga-labelled PSMA ligand HBED-CC in the diagnosis of recurrent prostate cancer. Eur J Nucl Med Mol Imaging 42:197–209
20. Prasad V, Steffen IG, Diederichs G et al (2016) Biodistribution of [^{68}Ga]PSMA-HBED-CC in patients with prostate cancer: characterization of uptake in normal organs and tumour lesions. Mol Imaging Biol 18:428–436
21. Pyka T, Okamoto S, Dahlbender M et al (2016) Comparison of bone scintigraphy and ^{68}Ga-PSMA PET for skeletal staging in prostate cancer. Eur J Nucl Med Mol Imaging 43:2114–2121
22. Dietlein M, Kobe C, Kuhnert G et al (2015) Comparison of [^{18}F]DCFPyL and [^{68}Ga]Ga-PSMA-HBED-CC for PSMA-PET imaging in patients with relapsed prostate cancer. Mol Imaging Biol 17:575–584
23. Ceci F, Castellucci P, Graziani T et al (2015) ^{11}C-choline PET/CT identifies osteoblastic and osteolytic lesions in patients with metastatic prostate cancer. Clin Nucl Med 40:e265–e270
24. Saad F, Clarke N, Colombel M (2006) Natural history and treatment of bone complications in prostate cancer. Eur Urol 49:429–440
25. Rafiei S, Komarova SV (2013) Molecular signaling pathways mediating osteoclastogenesis induced by prostate cancer cells. BMC Cancer 13:605
26. Sottnik JL, Keller ET (2013) Understanding and targeting osteoclastic activity in prostate cancer bone metastases. Curr Mol Med 13:626–639
27. Zhang J, Dai J, Qi Y et al (2001) Osteoprotegerin inhibits prostate cancer-induced osteoclastogenesis and prevents prostate tumor growth in the bone. J Clin Invest 107:1235–1244
28. Smith MR, Saad F, Coleman R et al (2012) Denosumab and bone-metastasis-free survival in men with castration-resistant prostate cancer: results of a phase 3, randomised, placebo-controlled trial. Lancet 379:39–46
29. Fogelman I (1980) Skeletal uptake of diphosphonate: a review. Eur J Nucl Med 5:473–476
30. Cook GJ, Fogelman I (2001) The role of nuclear medicine in monitoring treatment in skeletal malignancy. Semin Nucl Med 31:206–211
31. Ahmadzadehfar H, Azgomi K, Hauser S et al (2017) ^{68}Ga-PSMA-11 PET as a gatekeeper for the treatment of metastatic prostate cancer with 223Ra: proof of concept. J Nucl Med 58:438–444
32. Ghanem N, Uhl M, Brink I et al (2005) Diagnostic value of MRI in comparison to scintigraphy, PET, MS-CT and PET/CT for the detection of metastases of bone. Eur J Radiol 55:41–55
33. Rahbar K, Ahmadzadehfar H, Kratochwil C et al (2017) German multicenter study investigating ^{177}Lu-PSMA-617 radioligand therapy in advanced prostate cancer patients. J Nucl Med 58:85–90
34. Benesova M, Schafer M, Bauder-Wust U et al (2015) Preclinical evaluation of a tailor-made DOTA-conjugated PSMA inhibitor with optimized linker moiety for imaging and endoradiotherapy of prostate cancer. J Nucl Med 56:914–920
35. Okamoto S, Thieme A, Allmann J et al (2017) Radiation dosimetry for ^{177}Lu-PSMA I&T in metastatic castration-resistant prostate cancer: absorbed dose in normal organs and tumor lesions. J Nucl Med 58:445–450
36. Scarpa L, Buxbaum S, Kendler D et al (2017) The 68Ga/177Lu theragnostic concept in PSMA targeting of castration-resistant prostate cancer: correlation of SUVmax values and absorbed dose estimates. Eur J Nucl Med Mol Imaging 44:788–800

37. Lecouvet FE, El Mouedden J, Collette L et al (2012) Can whole-body magnetic resonance imaging with diffusion-weighted imaging replace Tc-99m bone scanning and computed tomography for single-step detection of metastases in patients with high-risk prostate cancer? Eur Urol 62:68–75
38. Woo S, Kim SY, Kim SH, Cho JY (2016) Journal club: identification of bone metastasis with routine prostate MRI: a study of patients with newly diagnosed prostate cancer. AJR Am J Roentgenol 206:1156–1163
39. Blazak JK, Thomas P (2016) Paget disease: a potential pitfall in PSMA PET for prostate cancer. Clin Nucl Med 41:699–700
40. Gykiere P, Goethals L, Everaert H (2016) Healing sacral fracture masquerading as metastatic bone disease on a 68Ga-PSMA PET/CT. Clin Nucl Med 41:e346–e347
41. Artigas C, Otte FX, Lemort M et al (2017) Vertebral hemangioma mimicking bone metastasis in ^{68}Ga-PSMA ligand PET/CT. Clin Nucl Med 42:368–370
42. Fendler WP, Calais J, Allen-Auerbach M et al (2017) ^{68}Ga-PSMA-11 PET/CT interobserver agreement for prostate cancer assessments: an international multicenter prospective study. J Nucl Med. doi:10.2967/jnumed.117.190827